Electronic Supplementary Material (ESI) for Soft Matter.
This journal is © The Royal Society of Chemistry 2020

# Electronic Supplementary Material

## Instantaneous tension measurements in droplet interface bilayers using an inexpensive, integrated pendant drop camera†

Justin Rofeh[a] and Luke Theogarajan[b]

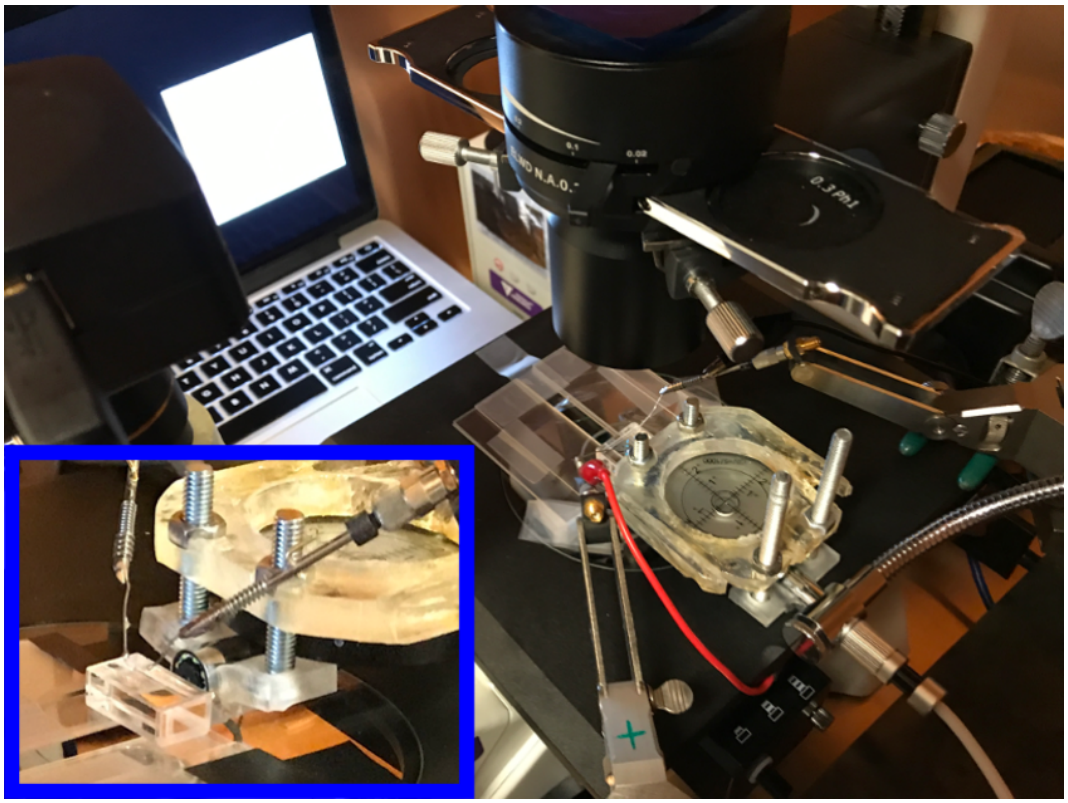

**Fig. S1** Photograph of the integrated pendant drop-microscope setup during a DIB experiment. The microscope camera is visible on the left, while the pendant drop camera is visible on the bottom right, held by a flexible metallic arm. A two-axis bubble level is fastened atop the shaft of the pendant drop camera by four nuts and bolts using 3D-printed parts. A long video of a white square on a laptop screen (background) is used as a source of diffuse light for the pendant drop camera. The fluorometer cuvette is immediately in front of the pendant drop camera, and two electrode wires are held over it by micropositioners. Red and black alligator clips connect these wires to the headstage of the Axopatch, which is affixed just beneath the microscope stage using a clamp. The entire setup is enclosed by a Faraday box with copper-colored sheet metal that is visible in the background. The box is closed during measurements to prevent outside sources of light from affecting image quality and to reduce the noise of capacitance measurements. The inset shows the cuvette, electrode wires, and pendant drop camera from a different angle.

[a] *Department of Physics, University of California, Santa Barbara, California 93106, USA*
[b] *Department of Electrical and Computer Engineering, University of California, Santa Barbara, California 93106, USA. E-mail: lusthe@ucsb.edu*

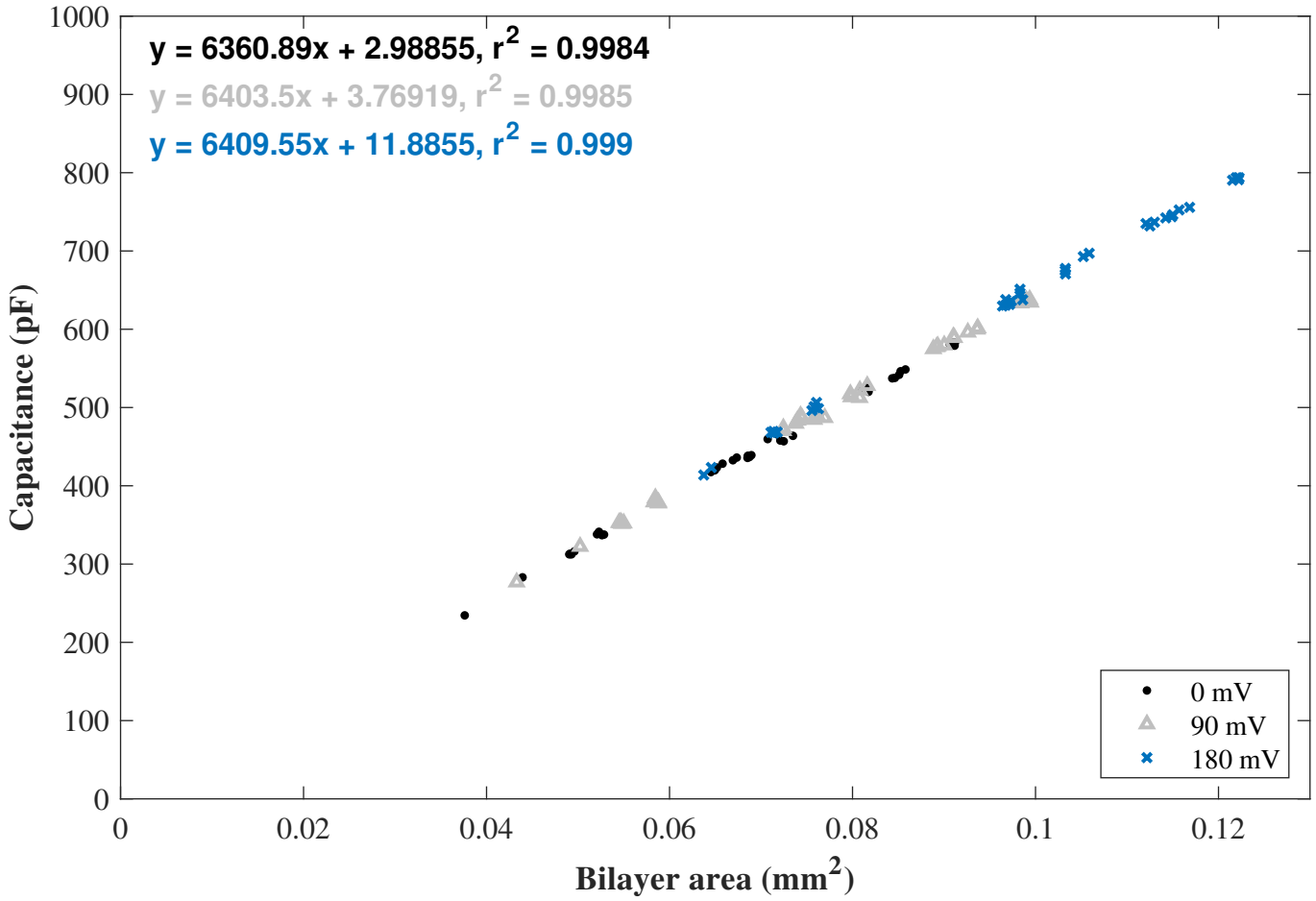


**Fig. S2** A replotting of the data set from Fig. 4 in the main text, which includes all trials in this study. This includes all of droplets 1-10 in Table S1 after contact. The specific capacitance as derived from the slope of the linear regression for the 0 mV data is 0.636 $\mu$F/cm$^2$, in good agreement with the mean of the individual specific capacitance values from Fig. 4, 0.641 $\pm$ 0.006 $\mu$F/cm$^2$.

## S1 Derivation of Young-Lippmann equation for a quadratic voltage dependence

The Lippmann equation is:

$$\frac{d\gamma_{\mathrm{b}}}{dV} = -\sigma(V)$$

where $\gamma_{\mathrm{b}}$ is the bilayer tension, $V$ is the applied voltage, and $\sigma(V)$ is the voltage-dependent double-layer charge per unit area[1–3]. From the definition of capacitance, $\sigma(V) = C_{\mathrm{s}}(V)V$, where $C_{\mathrm{s}}(V)$ is the voltage-dependent specific capacitance. $C_{\mathrm{s}}(V)$ is specified using the empirical relation $C_{\mathrm{s}}(V) = C_{\mathrm{s}}(0) + mV^2$ as described in the main text so that $\sigma(V) = [C_{\mathrm{s}}(0) + mV^2]V$. Inserting this into the Lippmann equation gives:

$$\frac{d\gamma_{\mathrm{b}}}{dV} = -[C_{\mathrm{s}}(0) + mV^2]V$$

We integrate this formula with respect to $V$ from $V = 0$ up to the applied voltage $V$:

$$\begin{aligned}\gamma_{\mathrm{b}}(V) - \gamma_{\mathrm{b}}(0) &= -\int_0^V [C_{\mathrm{s}}(0)V + mV^3]dV \\ &= -\frac{1}{2}C_{\mathrm{s}}(0)V^2 - \frac{1}{4}mV^4\end{aligned}$$

To obtain the modified Young-Lippmann equation, we insert Young's equation for a bilayer membrane $\gamma_{\mathrm{b}}(V) = 2\gamma_{\mathrm{m}}\cos[\theta(V)]$ into the above formula. Then we have:

$$2\gamma_{\mathrm{m}}\Big(\cos[\theta(0)] - \cos[\theta(V)]\Big) = \frac{1}{2}C_{\mathrm{s}}(0)V^2\big(1 + \frac{1}{2}\beta V^2\big)$$

where the substitution $\beta = m/C_{\mathrm{s}}(0)$ was used as described in the main text. This simplifies to the standard Young-Lippmann equation[3,4] if the capacitance is independent of voltage ($\beta = 0$). For the purposes of fitting data, this may be written as:

$$\cos[\theta(0)] - \cos[\theta(V)] = \frac{C_{\mathrm{s}}(0)}{4\gamma_{\mathrm{m}}}\big(1 + \frac{1}{2}\beta V^2\big)V^2$$

which is of the form $y = ax$ with $y = \cos[\theta(0)] - \cos[\theta(V)]$ and $x = \big(1 + \frac{1}{2}\beta V^2\big)V^2$. Then by performing a linear regression of a plot of $y$ with respect to $x$ at the value of $\beta$ for a particular system, the slope $a = \dfrac{C_{\mathrm{s}}(0)}{4\gamma_{\mathrm{m}}}$ is obtained.

# S2 Preparation of images and settings for pendant drop analysis

## S2.1 Calibration of the scale of the cameras

First the magnification of the pendant drop camera images was determined by identifying the horizontal extent of the droplet in the pendant drop camera with the horizontal extent of the droplet in the microscope camera. This is possible because both were set to be perpendicular to the droplets and because the microscope scale (3.172 pixels/μm) was determined using a known standard. This process was automated using a Matlab script based on edge detection and counting the number of pixels between the leftmost and rightmost edge. Care was taken to ensure that stray dirt or shadows outside the droplet region would not be mistaken as part of the droplets; this was verified by checking the scale of several images in every trial and then checking the deduced magnification of all other images for outliers. The scale of the pendant drop camera for all droplets in this work ranged from 0.53 to 0.62 pixels/μm.

## S2.2 Image cropping and brightness preparation

Prior to pendant drop fitting, the full-color pendant drop images were converted to grayscale. Then the Matlab function `imadjust` was used to increase the contrast by scaling the image intensity so that 1% of the pixels were saturated at white and black. This was done to increase the consistency of images taken with different optical settings. Additionally, images containing two droplets were cropped into images containing single droplets.

## S2.3 Settings for Pendant Drop software

When fitting solitary droplets using Pendant Drop, all parameters were left free to be fitted (tip radius, tip coordinates, capillary length, and gravity angle). The gravity angle is the angle of the direction of gravity relative to the orientation of the camera. This angle was generally near ~3° because we found it difficult to fasten the bubble level in the proper position when calibrating it with a homemade plumb bob. Still, the bubble level was also useful for ensuring that the camera was consistently maintained at a fixed orientation. Additionally, the bubble level was useful for leveling the other dimension of tilt by ensuring the bubble level lay flush with the shaft of the camera.

## S2.4 Setting a fit height (top width) for Pendant Drop software

Because there is no setting for the fitted region in Pendant Drop, the region to fit was determined by modifying the image prior to fitting. In order to set the top width of each image (the width of the droplet at the height up to which fitting is performed) a portion of the top of every image was cropped off prior to feeding it into Pendant Drop. This cropping was performed for both solitary droplets (for Method 1) and DIBs (for Method 3). If cropping is not performed prior to fitting solitary droplets, the software will consider the electrode profile to be a part of the droplet shape. For solitary droplets, the largest top width possible was used for each droplet. A top width of 250 μm was used for droplets 6-11. This corresponded to cropping the image through the waist of the ball electrode. A top width of 200 μm was used for droplets 1, 4, and 5, and a top width of 150 μm was used for droplets 2 and 3.

## S2.5 Setting a horizontal fit region for Pendant Drop software

In Method 3, the profile of only the outer half of each droplet in a DIB is fit using the Pendant Drop software. Again, because the Pendant Drop software does not allow a fitting region to be selected, mock symmetric images were formed using a Matlab script (`symmetrizer.m`) as shown in Fig. S3. The images of mock solitary droplets were created by flipping the outer portion of each droplet over a vertical axis going through the droplet bottoms. To accomplish this, first the mean gravity angle determined for fits of single droplets was used to rotate images of DIBs to become upright. Next, the edges were detected using a threshold above (below) which all pixels were white (black). Then Matlab's `edge` function was used to determine the droplet outline. Each image was then split into a left and right half near the bilayer region. Finally, the the outer side (the side not in contact) of each droplet was flipped over a vertical line going through the droplet bottom, to form a mock droplet with mirror symmetry.

In order to reduce errors associated with finding the droplet bottom, the Matlab script first detects the

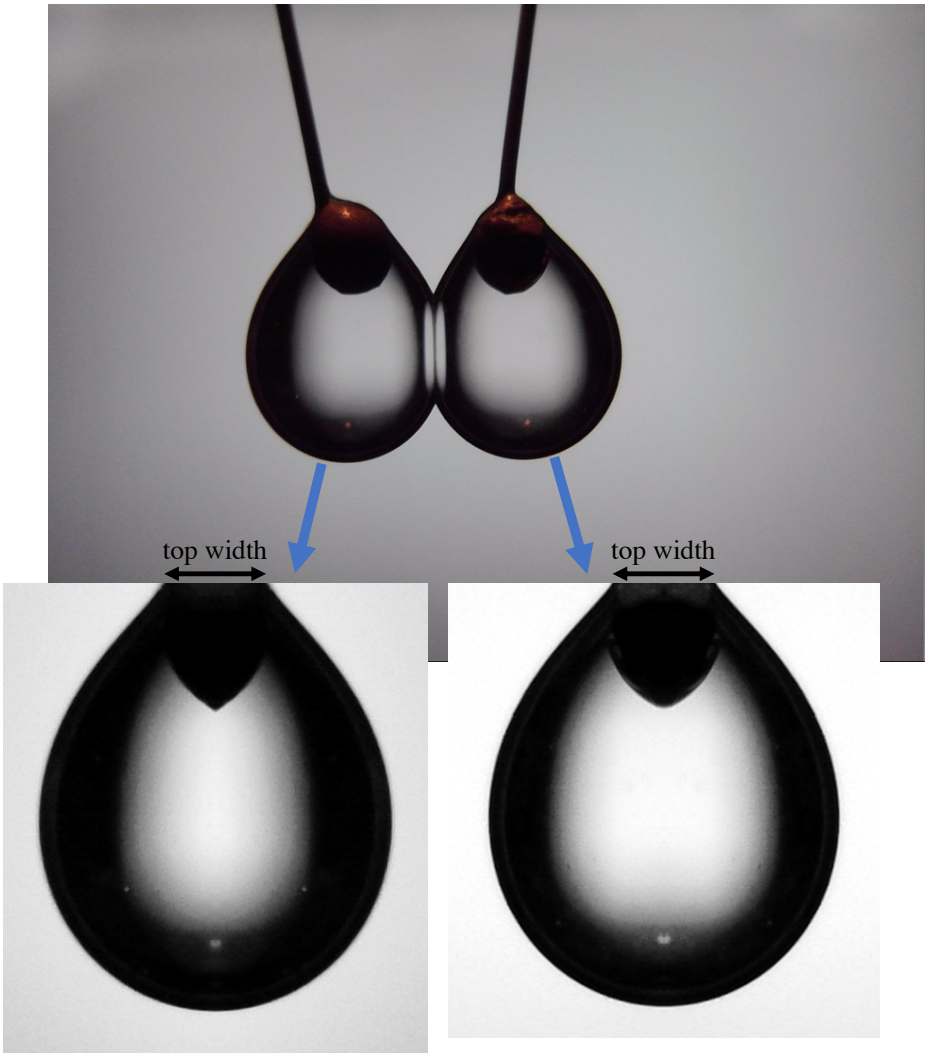


**Fig. S3** Demonstration of mock symmetric images generated by `symmetrizer.m` from an original raw image. The two mock symmetric images are fed directly into Pendant Drop in ImageJ. A top width of 200 μm was used in this example. As shown above, the top width refers to the width of the mock symmetric droplet rather than the droplet's true width in the DIB. The value of the top width must be smaller than the width of the droplet but larger than the width of the electrode in the mock symmetric image. Note the smoothness of the droplets at their bottoms.

bottom edge of each droplet, and then compares it with its mirror image about all points near the droplet bottom. The origin of reflection which yields a mirror image that is most similar to the original is selected as the origin of the flip transformation. The similarity between the original and its mirror image is calculated as the sum of vertical pixel distances between their edges. Care was taken to ensure half-pixel precision of the flip location (i.e. the flip origin can be situated between two pixels or in the middle of one pixel). It is important that these steps are performed after rotating the droplet image to ensure that it is upright; otherwise the resulting droplet shapes will be unrealistic. The symmetric mock droplet images were fed into Pendant Drop with all parameters set to be fitted except for the gravity angle, which was set to zero.

## S3 Detailed results for solitary droplets

**Table S1** Fits for solitary droplets using Pendant Drop. Each result is an average of N images.

| Droplet number | $V$ (nL) | Monolayer tension (mN/m) | Gravity angle (°) | RMS fit error (pixels) | $W$ | N | Note |
|---|---|---|---|---|---|---|---|
| 1 | 100 | 1.063 (0.028) | -2.80 (0.13) | 0.28 (0.02) | 0.31 | 6 | — |
| 2 | 100 | 1.115 (0.018) | -2.76 (0.03) | 0.44 (0.04) | 0.28 | 6 | — |
| 3 | 100 | 1.067 (0.036) | -2.99 (0.02) | 0.44 (0.01) | 0.26 | 8 | — |
| 4 | 150 | 1.086 (0.003) | -2.80 (0.02) | 0.33 (0.02) | 0.41 | 8 | — |
| 5 | 150 | 1.099 (0.005) | -2.43 (0.03) | 0.37 (0.05) | 0.34 | 8 | — |
| 6 | 200 | 1.113 (0.008) | -3.05 (0.01) | 0.33 (0.01) | 0.55 | 8 | — |
| 7 | 200 | 1.095 (0.022) | -2.70 (0.02) | 0.37 (0.01) | 0.60 | 8 | — |
| 8 | 200 | 1.105 (0.006) | -2.82 (0.01) | 0.26 (0.01) | 0.51 | 8 | — |
| 9 | 200 | 1.110 (0.005) | -3.02 (0.02) | 0.37 (0.02) | 0.55 | 8 | drop 9 before DIB formed |
| 10 | 200 | 1.121 (0.004) | -2.71 (0.02) | 0.33 (0.01) | 0.54 | 8 | drop 10 before DIB formed |
| 9B | 200 | 1.118 (0.010) | -2.97 (0.08) | 0.42 (0.06) | 0.53 | 8 | drop 9 separated after DIB |
| 10B | 200 | 1.116 (0.010) | -2.56 (0.07) | 0.50 (0.06) | 0.51 | 8 | drop 10 separated after DIB |
| 9C | 200 | 1.092 (0.004) | -3.24 (0.04) | 0.46 (0.02) | 0.54 | 8 | 9B with camera pitch → -1.2° |
| 10C | 200 | 1.102 (0.004) | -2.66 (0.03) | 0.42 (0.02) | 0.52 | 8 | 10B with camera pitch → -1.2° |
| 11 | 300 | 1.144 (0.005)[a] | -2.77 (0.02) | 0.35 (0.02) | 0.81 | 6 | non-equilibrium[a] |

[a] The 300-nL droplet fell off the electrode prior to reaching equilibrium. Therefore the measured monolayer tension sets an upper bound for its true value.

**Table S2** Fits for solitary droplets using Pendant Drop using different color settings for the pendant drop camera. For $\gamma_{RGB}$, the full color image was converted to grayscale and fed into Pendant Drop (i.e. the same preparation as Table S1). For e.g. $\gamma_{Red}$, only the red channel of each RGB image was used to generate a grayscale image.

| Droplet | $\gamma_{Full\ color}$ (mN/m) | $\gamma_{Red}$ (mN/m) | $\gamma_{Green}$ (mN/m) | $\gamma_{Blue}$ (mN/m) | N |
|---|---|---|---|---|---|
| 1 | 1.063 (0.028) | 1.065 (0.029) | 1.063 (0.027) | 1.057 (0.025) | 6 |
| 2 | 1.115 (0.018) | 1.115 (0.017) | 1.119 (0.017) | 1.120 (0.018) | 6 |
| 3 | 1.067 (0.036) | 1.063 (0.035) | 1.067 (0.035) | 1.068 (0.036) | 8 |
| 4 | 1.086 (0.003) | 1.086 (0.004) | 1.085 (0.003) | 1.085 (0.004) | 8 |
| 5 | 1.099 (0.005) | 1.092 (0.003) | 1.099 (0.005) | 1.104 (0.007) | 8 |
| 6 | 1.113 (0.008) | 1.114 (0.007) | 1.112 (0.008) | 1.111 (0.008) | 8 |
| 7 | 1.095 (0.022) | 1.092 (0.021) | 1.094 (0.022) | 1.104 (0.021) | 8 |
| 8 | 1.105 (0.006) | 1.106 (0.007) | 1.103 (0.006) | 1.109 (0.006) | 8 |
| 9 | 1.110 (0.005) | 1.108 (0.005) | 1.110 (0.005) | 1.114 (0.004) | 8 |
| 10 | 1.121 (0.004) | 1.120 (0.004) | 1.120 (0.003) | 1.124 (0.002) | 8 |

# S4 Accuracy of pendant drop measurements

We did not determine the error of our pendant drop measurements using a known standard because we could not find a well-characterized standard with a ~1-mN/m tension to use at the same volume and magnification settings as our DIB experiments. Instead, we sought to correct for any possible errors.

## S4.1 Radial distortion correction

Radial distortion is an aberration that increases with distance from the center of an image[5]. It arises from a nonideal lens shape. Examples include wheelbarrow and pincushion distortion, with an extreme example being a fish-eye lens. We were able to quantify the extent and effect of radial distortion using software. Images were taken of a chromium-on-glass photomask with 3-μm-wide parallel straight lines with 6-μm pitch. The lines filled the field of view of the camera, and images were taken with the lines both vertical and horizontal. Then the radial distortion parameters of the camera were determined by fitting using open source software (Hugin). The radial distortion is given by:

$$r_{\text{src}} = a r_{\text{dest}}^4 + b r_{\text{dest}}^3 + c r_{\text{dest}}^2 + (1 - a - b - c) r_{\text{dest}}$$

where $r_{\text{src}}$ is the normalized radius of a circle of points in an undistorted image and $r_{\text{dest}}$ is the resulting radius of the same set of points as a consequence of distortion[6,7]. At a magnification equivalent to 1.8 μm/pixel at the object plane, the fit parameters for our system are $a$ = 0.00145, $b$ = -0.00381 and $c$ = 0.0029. All single droplet images were then batch corrected for this aberration using the following Bash shell script using ImageMagick (via Terminal):

```
#!/bin/bash
for f in *.bmp
   do convert "$f" -distort barrel '0.00145 -0.00381 0.0029' converted/"$f"corrected.bmp
done
```

The difference between corrected and uncorrected images was not noticeable except for at the extreme corners of the images. Comparing the tensions of all droplets in Table S1 (i.e. all single droplet tension measurements in this work) for distortion-corrected and unaltered images, the mean difference was less than 0.05%. Therefore distortion correction was not used for any values reported in this work.

## S4.2 Chromatic aberration

Chromatic aberrations arise from the different indices of refraction for different colors of light in lenses[8]. Axial chromatic aberration results from different focal points of different wavelength of light; it consists of a defocusing effect of two color channels (e.g. red and blue) while another one (e.g. green) is in focus. Transverse chromatic aberration results from different magnifications for different wavelengths of light. As a result, the magnitude of axial chromatic aberration is constant over an entire image, while transverse chromatic aberration increases further from the image center[8].

In order to quantify errors associated with chromatic aberration, we have individually analyzed the different color channels of each RGB image used in Table S1. Beginning with the full color image from the pendant drop camera, first a single channel (red, green, or blue) was extracted from the image. Then this single channel was used to generate a grayscale image that was then fed into Pendant Drop. The results are shown in Table S2 for all three color channels. If chromatic aberration is significant, it would be expected that the different color channels would produce different results. However, the monolayer tensions resulting from all channels are usually within 0.5% of each other and always within 1.1% of each other. The mean absolute differences of tensions determined by comparing the single-channel images relative to each other are:

Red-Green: 0.19%
Green-Blue: 0.08%
Red-Blue: 0.36%

Considering these results, the up to 1.1% error between different channels is primarily a random error in relation to chromatic aberration, and the error due to chromatic aberration using our full color images is less than 0.5%.

### S4.3 Camera alignment

The pendant drop camera had an upward tilt of 0.4°-0.7° for all results reported here (Droplets 1-11 in Table S1) with the exception of Droplets 9C and 10C. In Droplets 9C and 10C the camera was deliberately tilted downwards 1.2° to determine its effect on the monolayer tension and gain a sense of the error due to tilt. Measurements on Droplets 1-8 and 11 were performed at an upward tilt of 0.7° while measurements on Droplets 9A-B and 10A-B were performed at an upward tilt of 0.4°. Comparing the monolayer tension of 200 nL droplets resulting from different camera tilts (Droplets 6, 7, 8, 9A-C, and 10A-C) shows that this tilt in the camera is unlikely to be responsible for an error greater than 2%.

The upward/downward tilt of the camera was measured using a bubble level mounted to the shaft of the camera, as shown in Fig. S1. The readings from the bubble level are only accurate if the shaft of the camera is coaxial with the camera and the bottom of the bubble level lies flush with the shaft. These properties are set by the manufacturer of the camera and bubble level; therefore we found it important to calibrate the mounted bubble level using the method demonstrated in Fig. S4. The screen of an iPhone 11 Pro Max was used as a mirror because it was straightforward to ensure it was upright. The iPhone 11 was fixed in a tripod and adjusted so that the screen was vertical relative to gravity using the gyroscope feature of an app named Bubble Level by Lemondo Entertainment. Using this method, the readings of the mounted bubble level were found to have an offset of 0.7° (range: 0.6°-0.9°) for measurements recorded at six different camera-mirror distances (range: 45 mm to 785 mm). This offset was used to correct the reported values of camera tilt (e.g. the bubble level read -1.9° for droplets 9C and 10C and we have corrected the value to -1.2°).

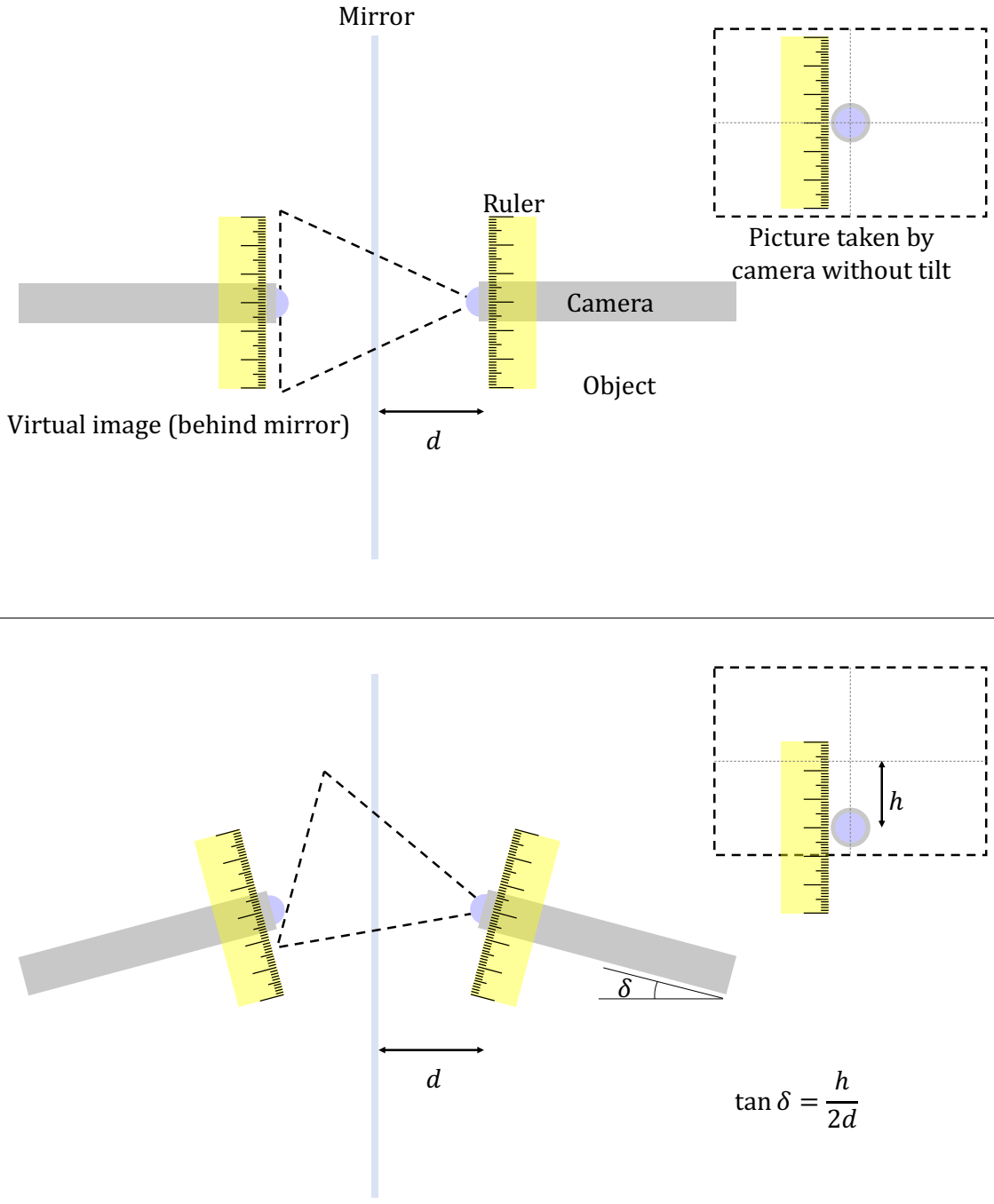


**Fig. S4** Demonstration of the test used to determine the magnitude of tilt of the pendant drop camera relative to the angle of gravity. The camera was held so that bubble level (not shown; mounted to the shaft of the camera) read <0.25°. Then a picture was taken. $\delta$ was measured for six different distances. E.g. a value of $h$ = 1.15 mm was measured for $d$ = 45 mm. This corresponds to an angle of $\delta$ = 0.73 ° using the formula $\tan\delta = \frac{h}{2d}$.

## S5 Determining bilayer contact angle, bilayer diameter, and droplet slant in DIBs

A Matlab script (`findangleanddiameter.m`) was coded to determine the bilayer diameter and four contact angles visible in the each DIB image. Examples of results figures output by the script are shown in Figs. S5, S6 and S7. As in `symmetrizer.m`, the script starts by converting the image to grayscale and scaling the image intensity via the `imadjust` function. Then, two different edge detection methods are used to determine the contact angle and diameter. The first, which we call the "Uncanny" edge, is used to determined the bilayer diameter. First, the image is converted to black and white by establishing an intensity threshold below (above) which all pixels are changed to black (white). This prevents the edge detection algorithm from detecting edges other than the droplet profile; this is critical for the automated detection of the contact points using the minimum and maximum of the detected edges. Then, edge detection is performed using Matlab's edge function with the "Canny" setting. This is not a true Canny edge detection because it is performed on a black and white image. This "Uncanny" edge is converted to a top and bottom edge: the first edge pixel found from the bottom (top) of the image is ascribed to the bottom (top) edge for every horizontal pixel location. The maximum of the bottom edge and the minimum of the top edge represent the locations of the top and bottom contact points. The distance in pixels between the top contact point and bottom contact point is used to determine the diameter in pixels. Then the scale of the camera is used to convert this into a physical length.

After the bottom and top contact points are located, a different edge detection is performed on the original grayscale DIB image (after imadjust is performed). We call this the Canny edge. This is a true Canny algorithm, because the original image is not first converted into black and white. Otsu's threshold[9,10] is used:

```
otsuthreshold = graythresh(DIBimage);
DIBimagecannyedge = edge(DIBimage,'Canny',otsuthreshold,otsuthreshold/2);
```

Because this algorithm sometimes detects stray edges away from the droplet profile, the previous Uncanny edge is used to determine to location of the fitting region by counting out pixels horizontally outward from the contact point. The same region in the Canny edge is then fit with a linear regression. To do this, first the detected Canny edge points are converted into ordered pairs. Then this set of ordered pairs is fit with a linear regression. The slope of the line is then converted into an angle relative to the vertical using the inverse tangent of the reciprocal of the slope. The bilayer contact angle calculation is performed for each of the four regions fitted in an image. These four values are averaged to produce a single contact angle.

We found that in the case of the pendant drop images, the detected Canny edge comprises of a single contiguous line near the contact points. But in the case of the microscope image, the detected Canny edge is fragmented. To solve this issue, the resolution of the microscope images is reduced by a factor of two in each dimension prior to edge detection. This results in the detection of a single contiguous line. The linear regressions are performed on the region between 5 μm and 15 μm (horizontally) from the bilayer; this corresponded to a 17-pixel-wide region in the case of the microscope camera and a 6- or 7-pixel-wide region in the case of the pendant drop camera (depending on the level of zoom of the camera). The quality of the fits to these regions was assessed via their associated $r^2$ values, which are output by the program.

Fig. S8 demonstrates the ability of the $r^2$ values to detect defects on the DIB surface. Due to our large data set, which includes thousands of images, we have rejected images automatically on the basis of their associated $r^2$ values. The calculation of mean contact angles was barely affected by the inclusion of images with defects; in this case, only microscope images with a minimum $r^2$ value below 0.92 were considered outliers mainly for the purpose of improving the aesthetics of Fig. 6 in the main text by excluding extreme outliers; no outliers were removed for the pendant drop camera images for this purpose. Because the calculation of tensions via electrowetting is more sensitive to errors, more restrictive criteria were used. If the mean of the minimum $r^2$ values for a sweep was less than 0.97 for the microscope camera or 0.90 for the pendant drop camera, the entire sweep was considered an outlier and excluded from the calculation.

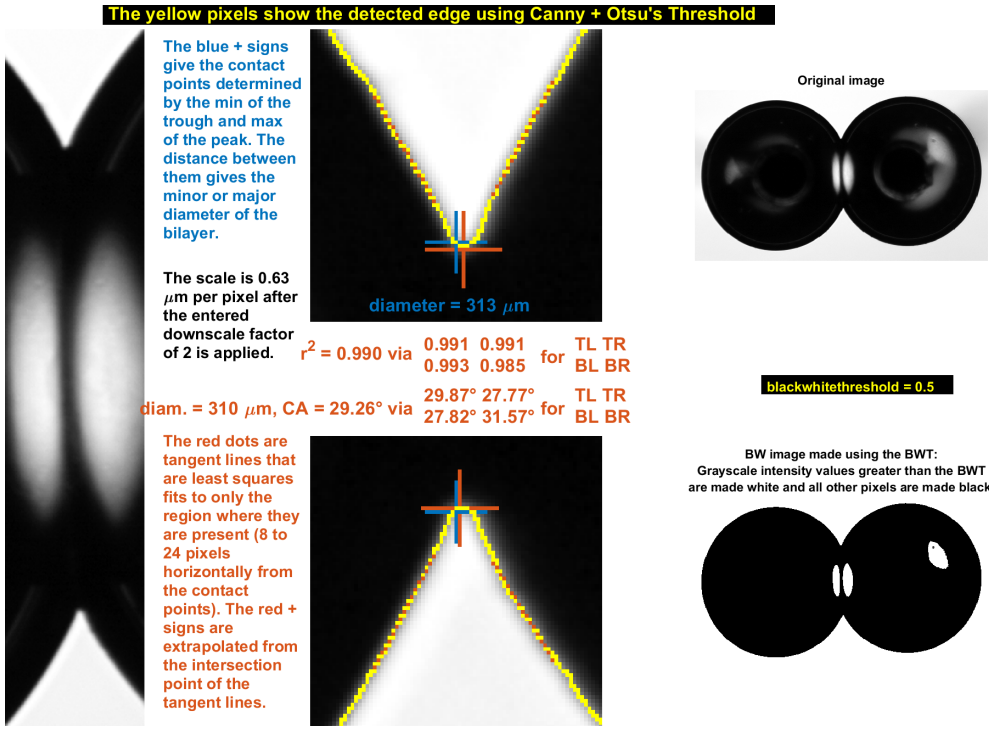


**Fig. S5** Figure output by `findangleanddiameter.m` for a microscope camera image taken at 0 mV simultaneously with that in Fig. S6.

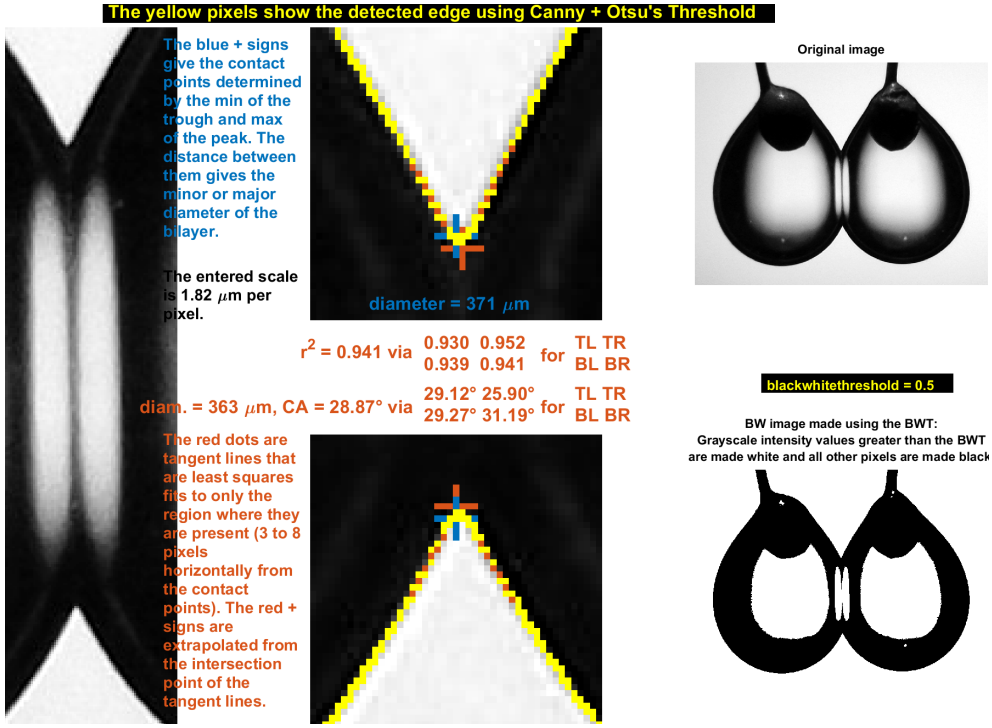


**Fig. S6** Figure output by `findangleanddiameter.m` for a pendant drop camera image taken at 0 mV simultaneously with that in Fig. S5.

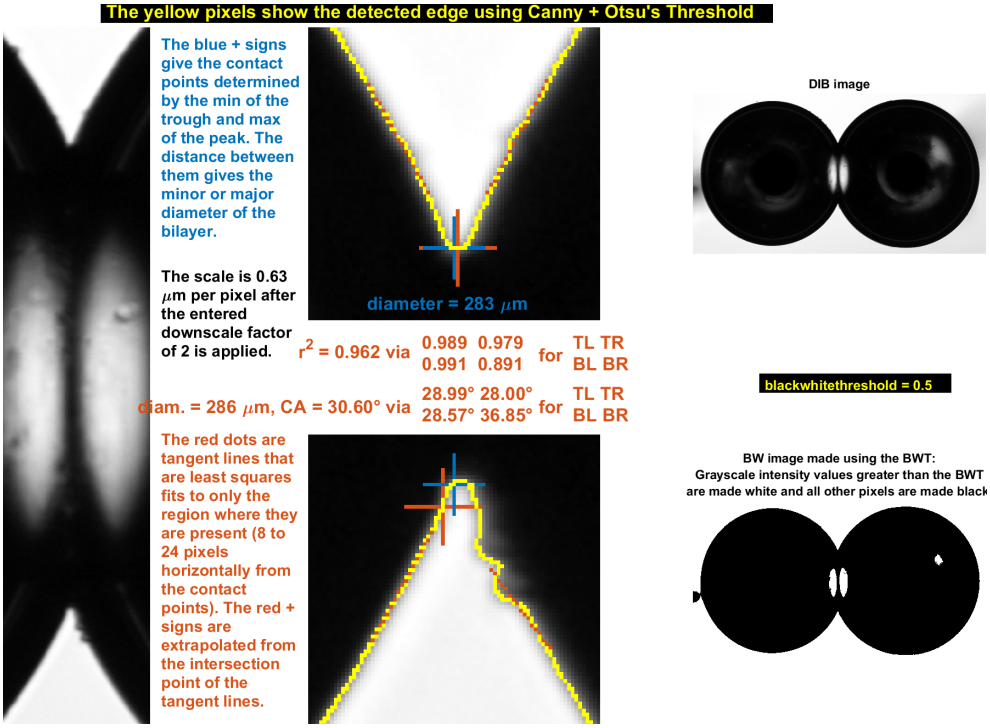


**Fig. S7** Figure output by `findangleanddiameter.m` for a microscope camera image taken at 0 mV in an experiment where defects were present in the fitting region. Each tangent line has a different amount of defects present. The $r^2$ value is 0.991 in the bottom left tangent line where no defects are noticeable, 0.989 in the top left where a defect is barely noticeably, 0.979 in the top left corner with a small defect, and 0.891 where there is a large defect. The smallest of these four $r^2$ values (the "minimum $r^2$ value" for the image) was used to determine whether it should be excluded from contact angle and tension calculations.

## S6 Determining droplet slant in DIBs

The algorithm for the droplet slant (filename: `asymmetrycalculator.m`) is similar to the contact angle algorithm. But rather than performing linear regressions of the DIB edge near the top and bottom contact points, linear regressions are performed only above the bilayer. Additionally, the regressions are performed on both the outer and inner side of each droplet. The fitted region on the inside of each droplet is found by counting out 20 μm (horizontally) from the contact point in either direction. Then a 60-μm region is fit (i.e. the DIB edge between 20 μm and 80 μm horizontally from the contact point). The corresponding region is found on the outside of the droplets by finding the points with the same height as the minimum of the interior regions (i.e. the same height as the points 20 μm from the contact point). The angles of the fitted tangent lines relative to the vertical were calculated from the slope of the linear regressions. Then the angles on either side of a droplet were subtracted to determine the slant of a droplet. Thus equal angles (i.e. a symmetric droplet) would result in a slant of zero. Finally, the slant in the left droplet and right droplet were subtracted from each other (Note: the slant of each droplet is signed so subtraction increases the magnitude of the slant unless the droplets are slanted in the same direction.). Only the Uncanny edge is used in this algorithm because the fitted region is much larger and therefore not sensitive to the edge detection method.

## S7 Effect of fitting region on contact angles and deduced monolayer and bilayer tensions

In this section, we aim to highlight the ambiguity in the choice of the region over which to perform the linear regressions that determine the tangent lines near the contact interface. Naively, the fit region from 0 to 10 μm from the contact interface would be an ideal choice, but there are three arguments against this:

1.) The region immediately surrounding the contact point has a nonphysical shape that appears rounded when zooming in, as evident in Figs. S5 and S6. Other authors have noted similar effects in sessile drop goniometry, and attributed them to effects such as diffraction and scattering[11,12].

2.) Defects tend to accumulate on and straddle the contact line as shown in Fig. S7. These have the effect of biasing the contact angle measurements. These defects are also present away from the contact line, but in these regions, their effect averages to zero. Similar defects have been noted as a source of "optical noise" in captive bubble experiments[13].

3.) The monolayer tension calculated via the electrowetting approach is obviously too low when this fitting region is used in the case of the pendant drop camera ($0.91 \pm 0.119$ mN/m). This is based on comparison with the value of 1.11 mN/m determined via Young-Laplace shape analysis, which we have shown is accurate to within a few percent.

Determining the ideal region for fitting would require a study that is outside the scope of this paper. Without this knowledge, our choice of fitting region is somewhat ambiguous. To estimate the potential for errors stemming from a nonideal choice in fitting region, we have calculated mean contact angles for the same set of images as in Fig. 6 in the main text for three different choices of fitting region: the region from 1 μm to 11 μm, the region from 5 μm to 15 μm, and the region from 9 μm to 19 μm from the contact interface. The resulting data is shown in Tables S3 and S4.

The tables show a 13% range in the mean contact angle at 0 mV and a 30% range in the associated monolayer tension deduced using the Young-Lippmann equation when both cameras are considered. The contact angles deduced from the region from 9 μm to 19 μm are ∼1° higher than those for the region from 5 μm to 15 μm. Extrapolating from this observation, we can expect that the true values for the region from 1 μm to 11 μm might be ∼1° lower than those for the region from 5 μm to 15 μm. Relative to this extrapolation, the contact angles for the 1 μm to 11 μm region are ∼1° lower for the microscope camera and ∼1° higher for the pendant drop camera, which suggests that the calculations resulting from this fit region are not accurate.

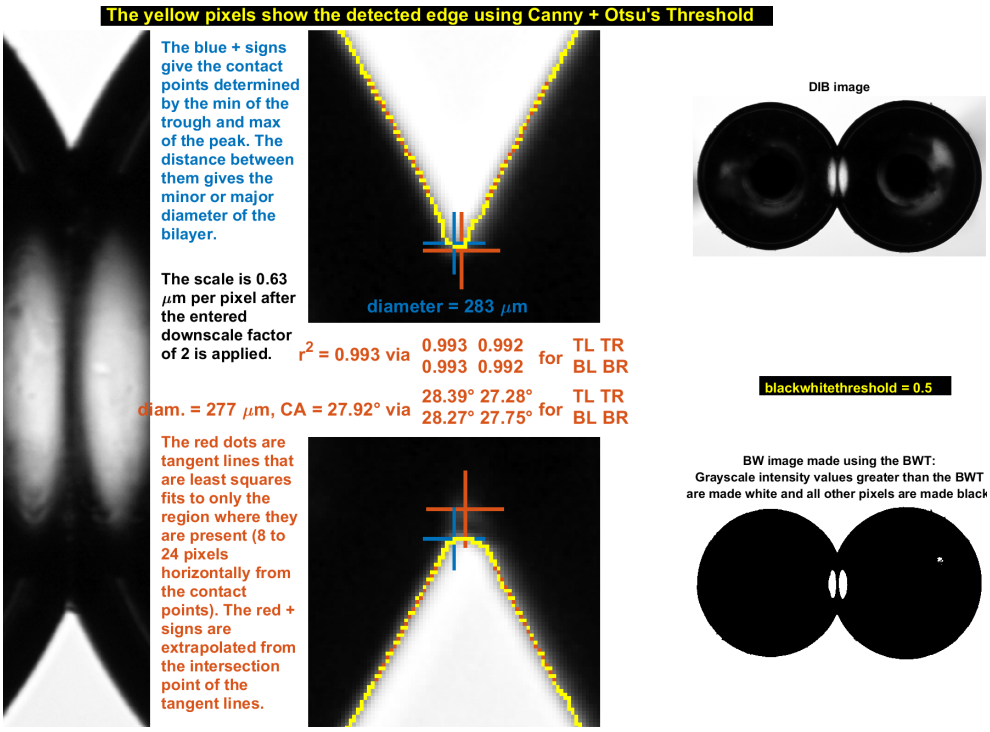


**Fig. S8** Figure output by `findangleanddiameter.m` for a microscope camera image taken at 0 mV in an experiment where defects were present along the bilayer contact interface.

| Fit region | $\theta$(0 mV) (°) | $\theta$(180 mV) (°) | $\gamma_m$ (mN/m) | $\gamma_b$ (mN/m) | $N_{sweeps}$ ($r^2 > r_{threshold}$) |
|---|---|---|---|---|---|
| 1 to 11 μm | 27.6 (0.82) | 34.1 (1.34) | 0.91 (0.119) | 1.61 (0.208) | 24 |
| 5 to 15 μm | 27.7 (0.60) | 33.3 (0.73) | 1.04 (0.078) | 1.84 (0.138) | 33 |
| 9 to 19 μm | 28.4 (0.68) | 33.6 (0.84) | 1.13 (0.135) | 1.99 (0.236) | 34 |

**Table S3** Mean contact angles at 0V for all experiments in this study determined using the pendant drop camera images. If the $r^2$ of an image in a sweep was too low, the entire sweep was excluded from the mean for both the pendant drop camera and the microscope camera to avoid biasing the results from either camera. Low $r^2$ values corresponded with the presence of defects such as those present in Fig. S7. $\gamma_m$ and $\gamma_b$ were calculated via the electrowetting approach described in the main text.

| Fit region | $\theta$(0 mV) (°) | $\theta$(180 mV) (°) | $\gamma_m$ (mN/m) | $\gamma_b$ (mN/m) | $N_{sweeps}$ ($r^2 > r_{threshold}$) |
|---|---|---|---|---|---|
| 1 to 11 μm | 26.2 (1.25) | 31.7 (0.80) | 1.08 (0.136) | 1.94 (0.243) | 24 |
| 5 to 15 μm | 28.4 (0.67) | 33.4 (1.02) | 1.15 (0.100) | 2.02 (0.176) | 33 |
| 9 to 19 μm | 29.7 (0.60) | 34.5 (0.96) | 1.18 (0.119) | 2.05 (0.206) | 34 |

**Table S4** Mean contact angles at 0V for all experiments in this study determined using the microscope camera images.

## Notes and references


1 G. Lippmann, *PhD thesis*, Gauthier-Villars Paris, France:, 1875.

2 F. Mugele and J.-C. Baret, *Journal of Physics: Condensed Matter*, 2005, **17**, R705–R774.

3 J. Requena and D. Haydon, *Journal of Colloid and Interface Science*, 1975, **51**, 315–327.

4 G. J. Taylor, G. A. Venkatesan, C. P. Collier and S. A. Sarles, *Soft Matter*, 2015, **11**, 7592–7605.

5 *Distortion (optics) - Wikipedia*, `https://en.wikipedia.org/wiki/Distortion_(optics)`, (Accessed on 10/06/2019).

6 *Lens correction model - PanoTools.org Wiki*, `http://hugin.sourceforge.net/docs/manual/Lens_correction_model.html`, (Accessed on 10/06/2019).

7 *Lens Correction – IM v6 Examples*, `http://www.imagemagick.org/Usage/lens/`, (Accessed on 10/06/2019).

8 *Chromatic aberration - Wikipedia*, `https://en.wikipedia.org/wiki/Chromatic_aberration`, (Accessed on 10/06/2019).

9 S. F. Chini and A. Amirfazli, *Colloids and Surfaces A: Physicochemical and Engineering Aspects*, 2011, **388**, 29–37.

10 *Canny edge detector - Wikipedia*, `https://en.wikipedia.org/wiki/Canny_edge_detector`, (Accessed on 10/06/2019).

11 C. Dorrer and J. Rühe, *Langmuir*, 2006, **22**, 7652–7657.

12 C. Dorrer and J. Rühe, *Soft Matter*, 2009, **5**, 51–61.

13 Y. Y. Zuo, C. Do and A. W. Neumann, *Colloids and Surfaces A: Physicochemical and Engineering Aspects*, 2007, **299**, 109–116.